Electronic Supplementary Information (ESI)

Copper and Conjugated Carbonyls of Metal-organic Polymer as Dual Redox Centers for Na Storage

Liubin Wang,[a]* Ningbo Liu,[a] Xiaoying Zhao,[a] Xiaohan Wang,[a] Tong Zhang,[c] Zhiqiang Luo,[b]* and Fujun Li[c]*

[a]College of Chemistry & Materials Science, Key Laboratory of Analytical Science and Technology of Hebei Province, Hebei University, Baoding 071002, China

[b]Tianjin Key Lab for Photoelectric Materials & Devices, School of Materials Science and Engineering, Tianjin University of Technology, Tianjin 300384, China

[c]Frontiers Science Center for New Organic Matter, Key Laboratory of Advanced Energy Materials Chemistry (Ministry of Education), Renewable Energy Conversion and Storage Center (RECAST), College of Chemistry, Nankai University. Tianjin 300071, China

Experimental

Materials: Potassium phthalimide (Sigma-Aldrich, 98.0%), Tetrachloro-p-benzoquinone (Aladdin, 98%), dimethyl sulfoxide (DMSO, Aladdin, 99.5%), N,N-Dimethylformamide (DMF, Aladdin, 99.5%), hydrazine hydrate (Heowns, 80.0wt%), $Cu(NO_3)_2 \cdot 3H_2O$ (Aladdin, 99%), acetonitrile (Macklin, 99.5%), and ammonia solution (Damao, 25%) were purchased and used without further purification. Tetramino-benzoquinone (TABQ) was synthesized through two-step reactions according to the literature.[S1]

Synthesis of Cu-TABQ: Cu-TABQ was synthesized by a simple solution method (Fig. S1). $Cu(NO_3)_2 \cdot 3H_2O$ (1mmol) was dissolved in 30 mL DMSO and 3 mL of concentrated aqueous ammonia (~14 M), after that, it was added to DMSO solution with 1mmol TABQ under vigorous stirring. The reaction was kept with stirring for 3 h under ambient air at 30°C, 60°C, and 90°C, respectively. The solid was thoroughly washed with deionized H_2O, DMSO, and acetone several times, and then dried at 90 °C in an oven for 12 h. Finally, Cu-TABQ with different morphologies was obtained.

Material Characterization: Powder X-ray diffraction (XRD, Rigaku MiniFlex600 X-ray generator, Cu Kα radiation, $\lambda = 1.5406$ Å) and high-resolution transmission electron microscopy (HRTEM) (Taols F200X G2, AEMC) were applied to investigate the crystallinity of the Cu-TABQ powder. The spectroscopic characteristics of Cu-TABQ were revealed with Fourier transform infrared spectroscopy (FTIR, ThermoFisher Scientific Nicolet iS10), Raman spectroscopy (Raman, HORIBA, LabRAM HR Evolution) with a laser wavelength of 532 nm, X-ray photoelectron spectroscopy (XPS, Perkin Elmer PHI 1600 ESCA, Perkin-Elmer) and solid-state 1H NMR with Inova 400MHz Spectrometer (Varian Inc., USA). In XPS spectra of materials, all binding energies were corrected using carbon element with a binding energy of C 1s = 284.6 eV as an internal standard. X-band electron paramagnetic resonance (EPR) spectra were obtained on a Bruker EMS nano spectrometer at room temperature.

Scanning electron microscopy (SEM, JEOL JSM-7500F) and transmission electron microscope (TEM, FEI TECNAI G2) were used to observe the crystal morphologies and microstructures with elemental mapping, and N_2 adsorption/desorption measurement (Quantachrome Autosorb-iQ-MP). Thermogravimetric analysis (TGA) was evaluated on TG/DTA STA449C thermal analyzer in airflow at a heating rate of 10 °C min^{-1} from ambient temperature to 800 °C.

Electrochemical measurements: The electrochemical performance of Cu-TABQ electrode was tested by Galvanostatic charge/discharge, cyclic voltammetry (CV), and rate, which were proved by CR2032-type coin cells at room temperature. The glass microfiber membrane (Whatman GF/D, Aldrich), 1.0 M NaPF6/DEGDME solution, and sodium foil were used as the separator, the electrolyte, and the anode, respectively. The preparation of Cu-TABQ working electrode was mixing Cu-TABQ, conductive carbon (Super P), and polyvinylidene fluoride (PVDF) at the weight ratio of 8: 1: 1 with anhydrous N-methyl-2-pyrrolidinone (NMP) solvent, the following pasted onto Al foil and drying at 80 °C in a vacuum oven for 12 h. The batteries were assembled in a glove box filled with an argon atmosphere (water and oxygen level under 1.0 ppm). Galvanostatic charge/discharge was performed on the LAND-CT2001A battery instrument (LAND Electronic Co., Wuhan China) between a voltage range of 1.0-3.0 V (vs. Na^+/Na) at room temperature. Cyclic voltammetry (CV) was conducted on the CHI 760E electrochemical workstation.

Computational details and Calculation of diffusion kinetics:

DFT calculations were performed using the Vienna Ab-initio Simulation Package (VASP).[S2, S3] The generalized gradient approximation (GGA) with the Perdew-Burke-Ernzerhof (PBE) functional was adopted to describe the electronic exchange and correlation effects.[S4, S5] The cutoff energy was set to 450 eV for both geometry optimization and self-consistent field computation. The convergence criterion of the total energy and force was set to 10^{-5} eV and 0.02 eV $Å^{-1}$, respectively. In the GITT test, the current pulse lasted for 20 min at 50 mA g^{-1} and then the cell was relaxed for

80 min to make the voltage reach the equilibrium. These procedures were repeatedly applied to the cell during the entire discharge/charge process. The Na^+ diffusion coefficients in the Cu-TABQ cathode were calculated from the GITT data by following formula [S6]:

$$D_{GITT} = \frac{4}{\pi}\left(\frac{m_B V_m}{M_B S}\right)^2 \left(\frac{\Delta E_s}{\tau(dE_\tau/d\sqrt{\tau})}\right)^2 \approx \frac{4}{\pi\tau}\left(\frac{m_B V_m}{M_B S}\right)^2 \left(\frac{\Delta E_s}{\Delta E_\tau}\right)^2 \left(\tau \ll \frac{L^2}{D_{GITT}}\right)$$

Where D_{Na+} ($cm^2\ s^{-1}$) means the chemical diffusion coefficient, τ is the constant current duration time (20 min), m_B is the mass of active material, M_B is the molecular weight ($g\ mol^{-1}$) and V_m is its molar volume ($cm^3\ mol^{-1}$), S is the total contacting area of electrode with electrolyte (1.1304 cm^2), and ΔE_s and ΔE_τ are the change in the steady state voltage and overall cell voltage after the application of a current pulse in a single step GITT experiment, respectively.

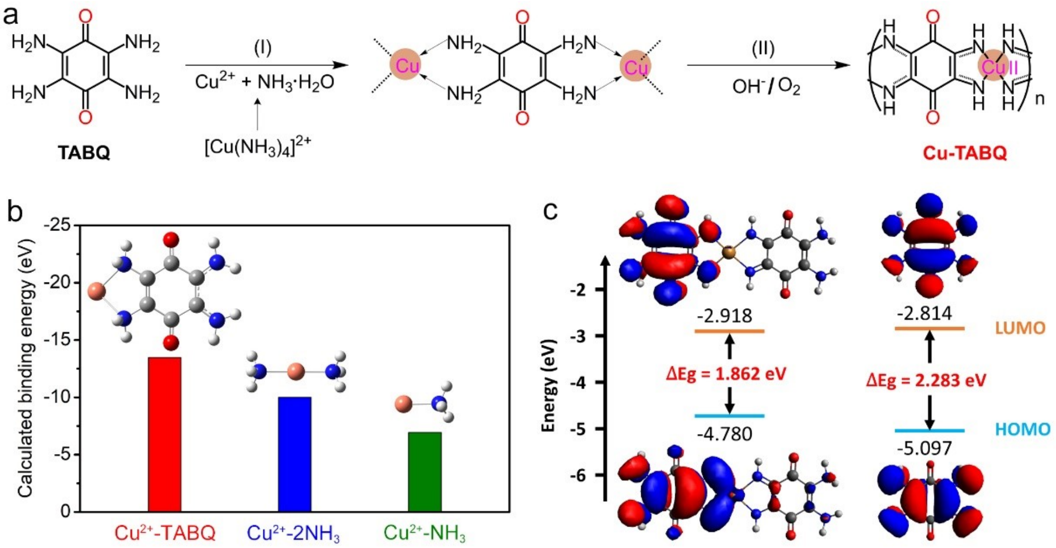

Fig. S1 (a) Schematic diagram of possible formation of Cu-TABQ; (b) the calculated binding energies of Cu^{2+}-TABQ, Cu^{2+}-$2NH_3$, and Cu^{2+}-NH_3; (c) HOMO/LUMO energy levels and orbits distributions of Cu-TABQ and TABQ.

The dissociated Cu^{2+} from $[Cu(NH_3)_4]^{2+}$ coordinated with the amidogen of the TABQ molecule and then stabilized by oxidative dehydrogenation under the assistance of O_2 and OH^-. Then, the coordination chains extend to grow with the slow release of Cu^{2+} from $[Cu(NH_3)_4]^{2+}$ to form Cu-TABQ. Density functional theory (DFT) is employed to analyse the lowest unoccupied molecular orbital (LUMO) and highest occupied molecular orbital (HOMO) energy levels of Cu-TABQ and TABQ in Figure S1c. A higher HOMO value represents a lower ionization potential and better reducibility. The lower LUMO value expresses better electron acceptance and excellent oxidation capability. Meanwhile, the smaller LUMO-HOMO gap (ΔEg) means an enhanced electronic delocalization. Compared with TABQ, Cu-TABQ presents lower LUMO energy level and narrow HOMO-LUMO energy gap (ΔEg), indicating the increased electron-accepting capability, thus resulting in the desirable electrochemical performance.

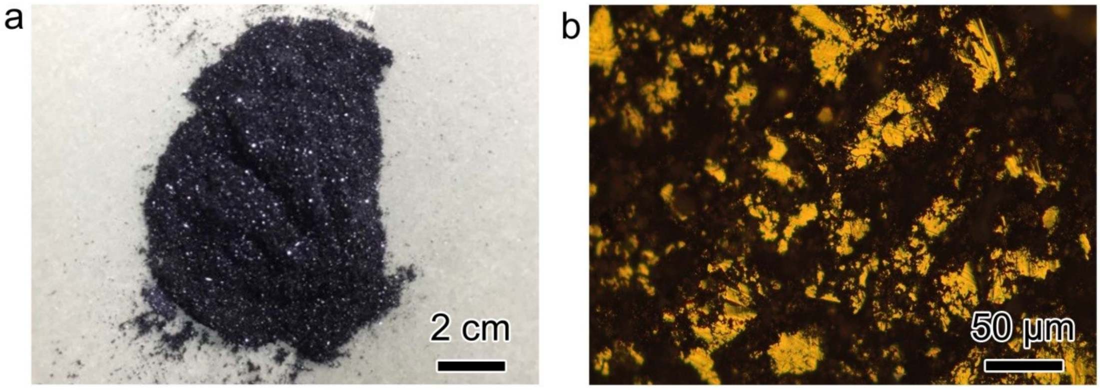

Fig. S2 Optical pictures of Cu-TABQ powders.

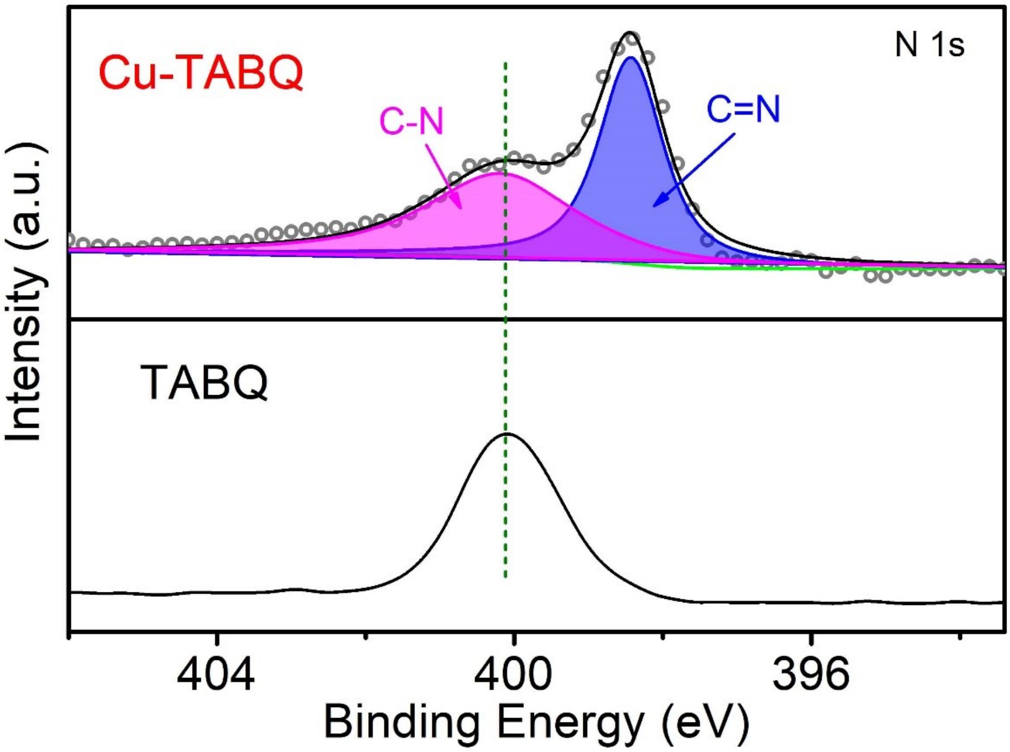

Fig. S3 N 1s XPS spectra of Cu-TABQ and TABQ.

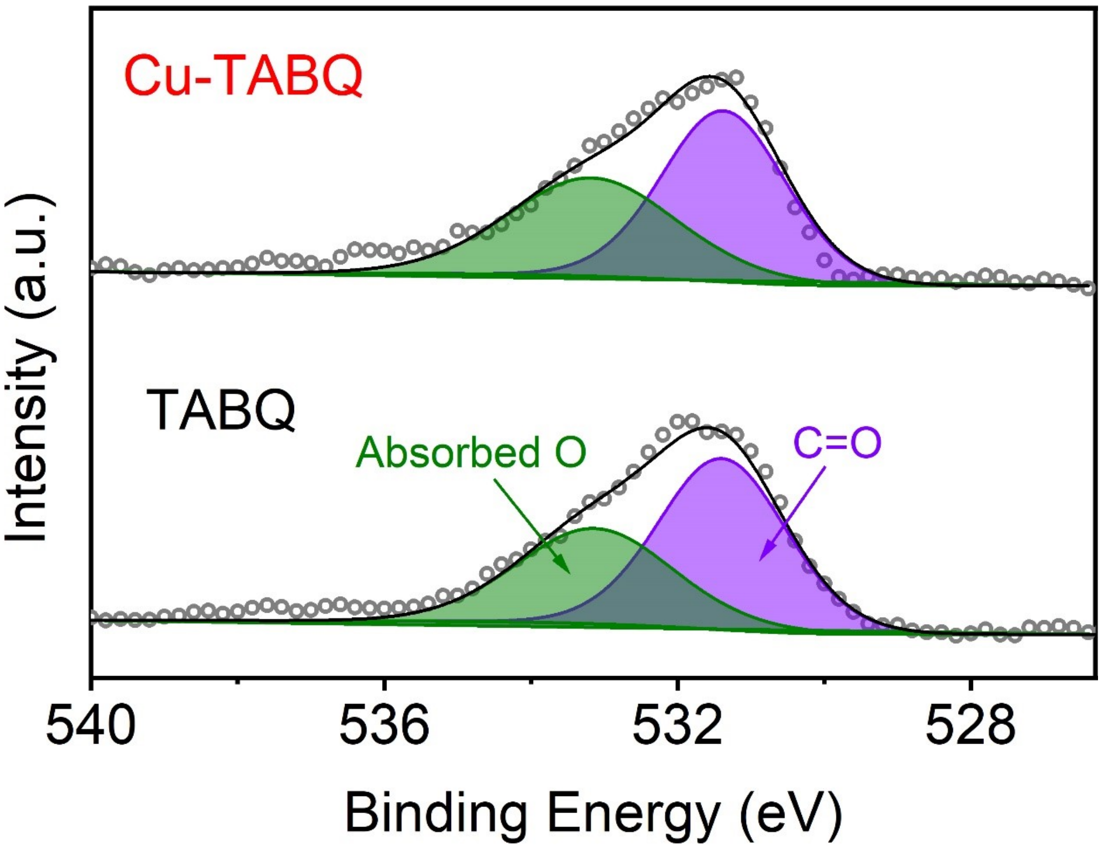

Fig. S4 O 1s XPS spectra of Cu-TABQ and TABQ.

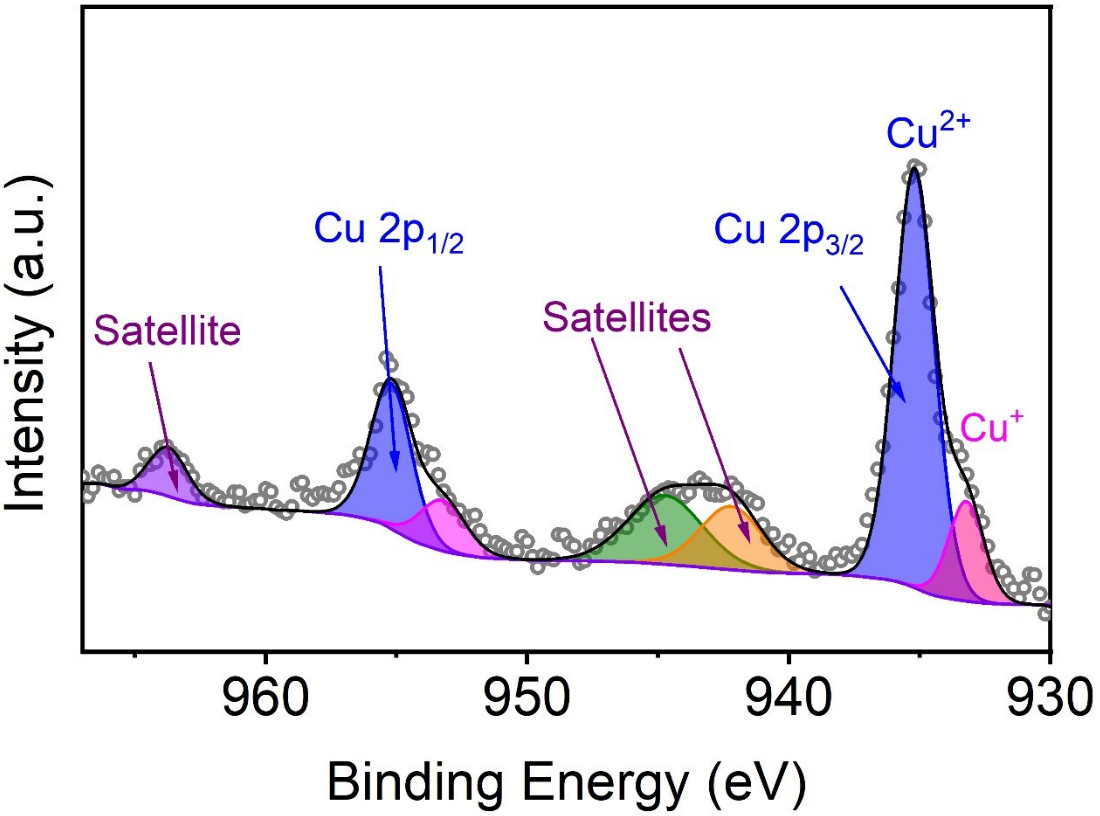

Fig. S5 Cu 2p XPS spectra of Cu-TABQ.

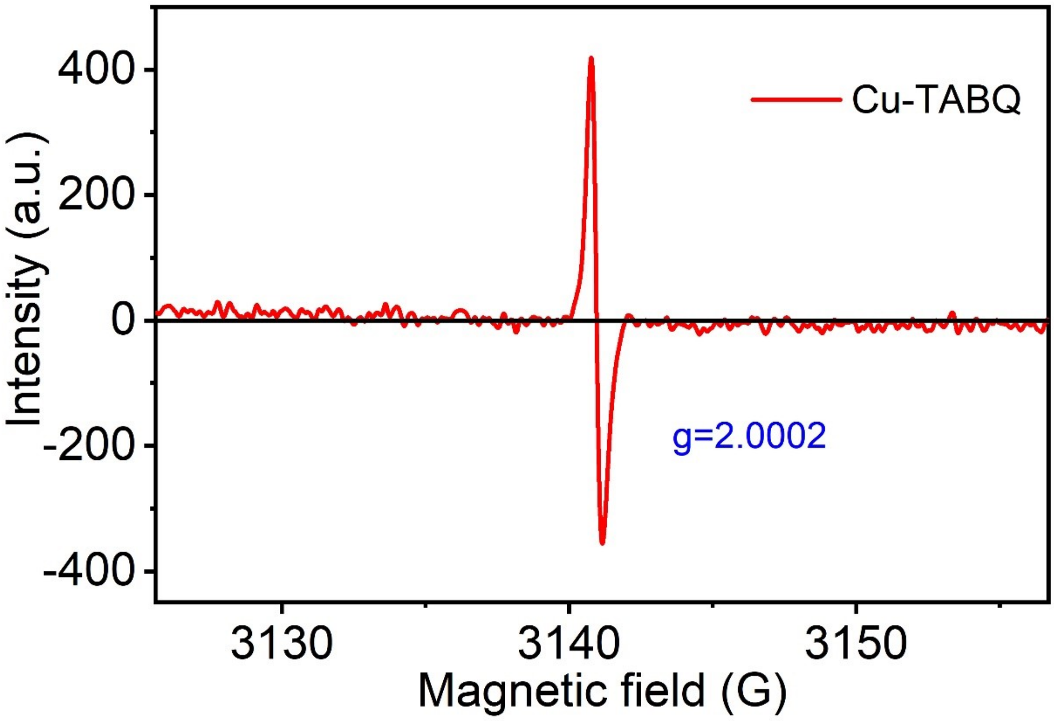

Fig. S6 EPR spectra of Cu-TABQ.

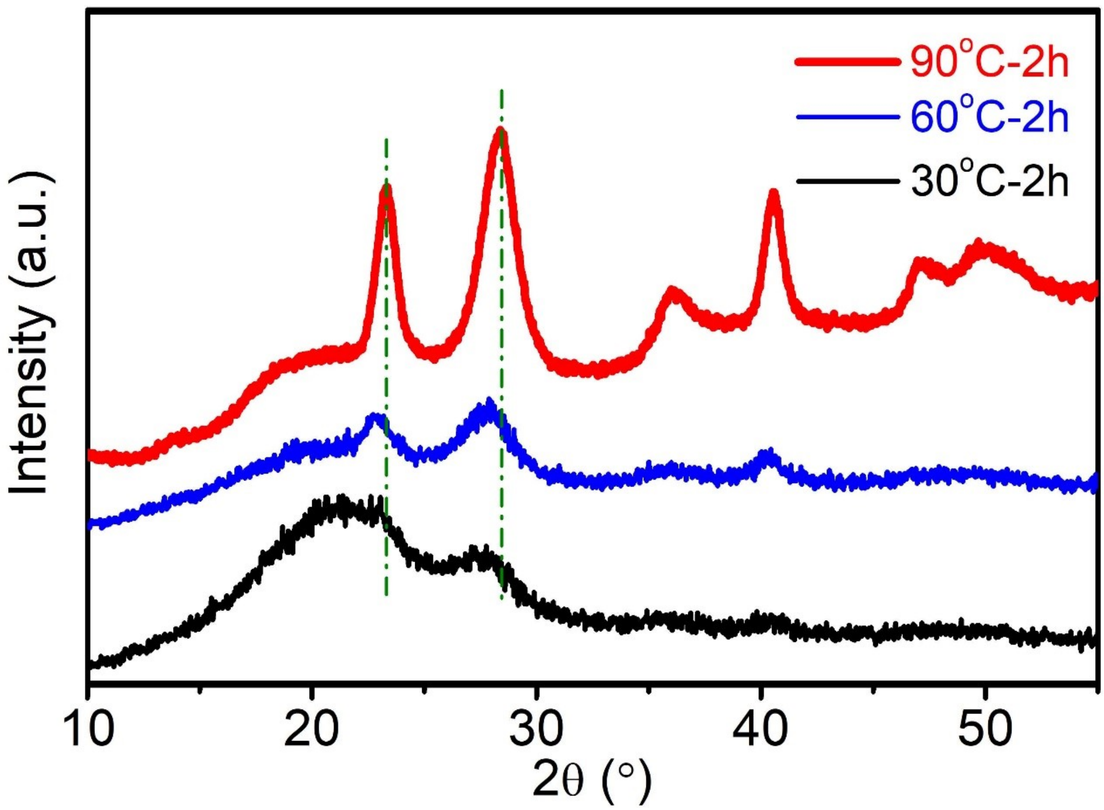

Fig. S7 XRD patterns of Cu-TABQ prepared at different reaction conditions.

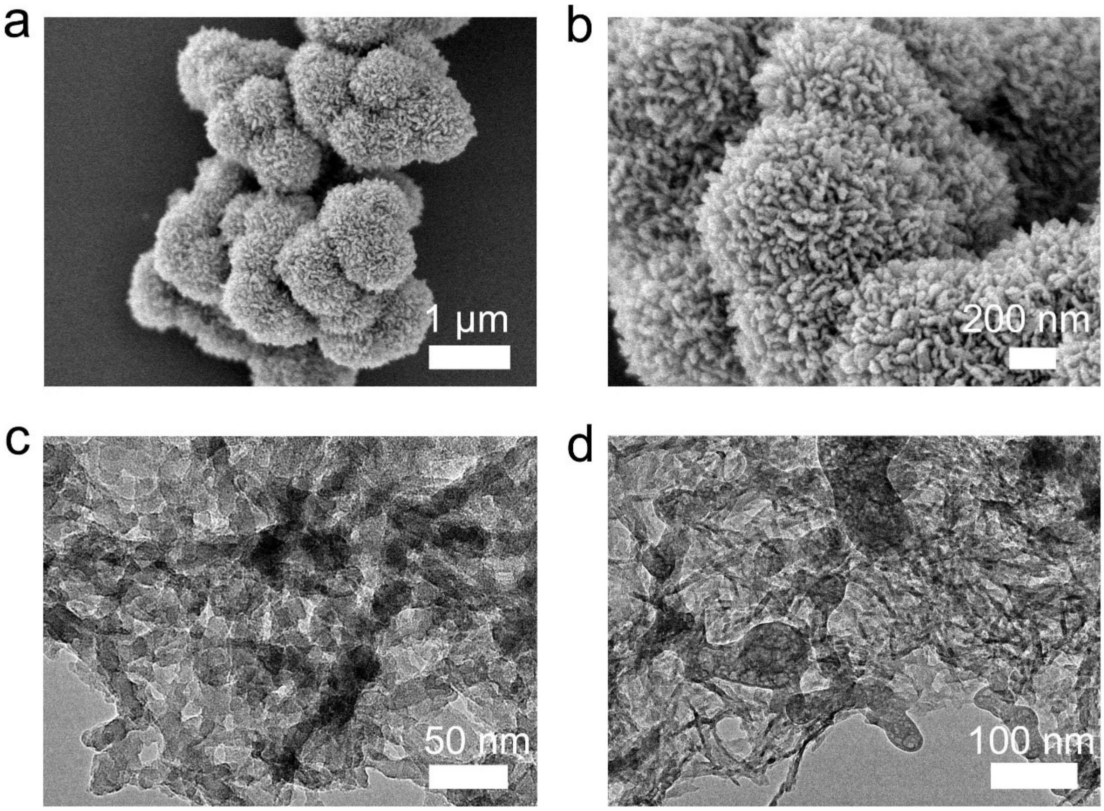

Fig. S8 (a,b) SEM and (c,d) TEM images of Cu-TABQ obtained at room temperature (30 ℃).

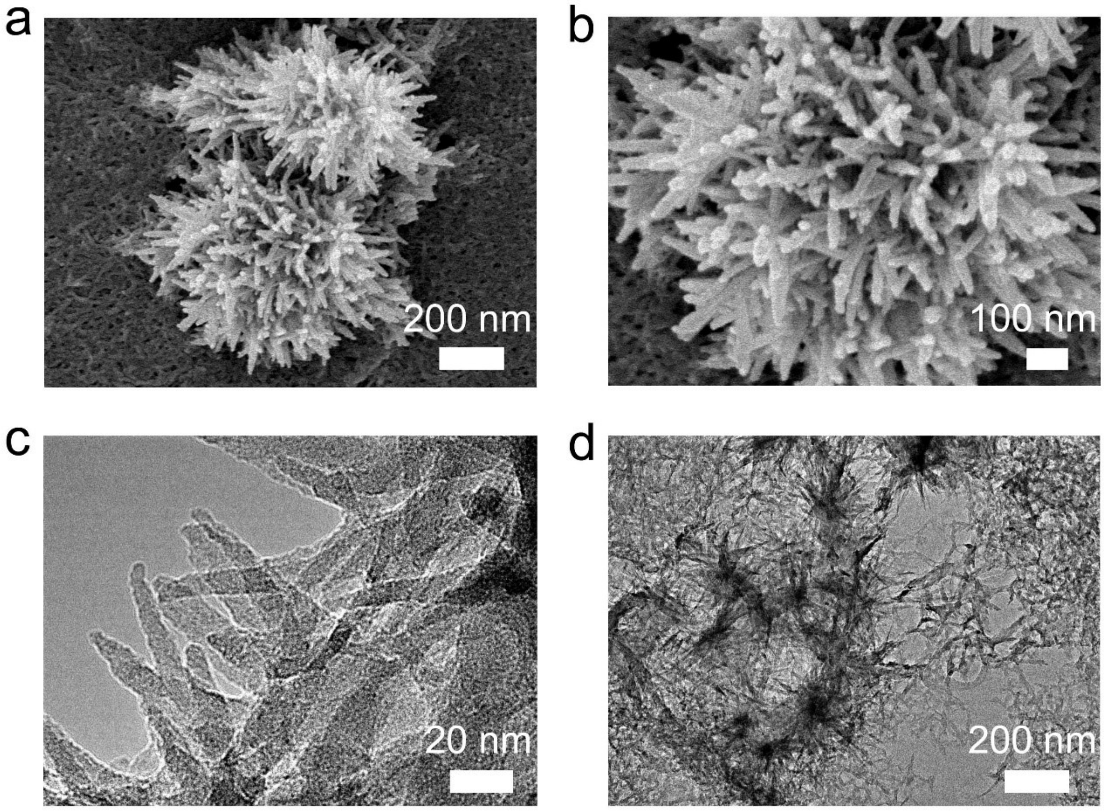

Fig. S9 (a,b) SEM and (c,d) TEM images of Cu-TABQ obtained via reaction at 60 °C.

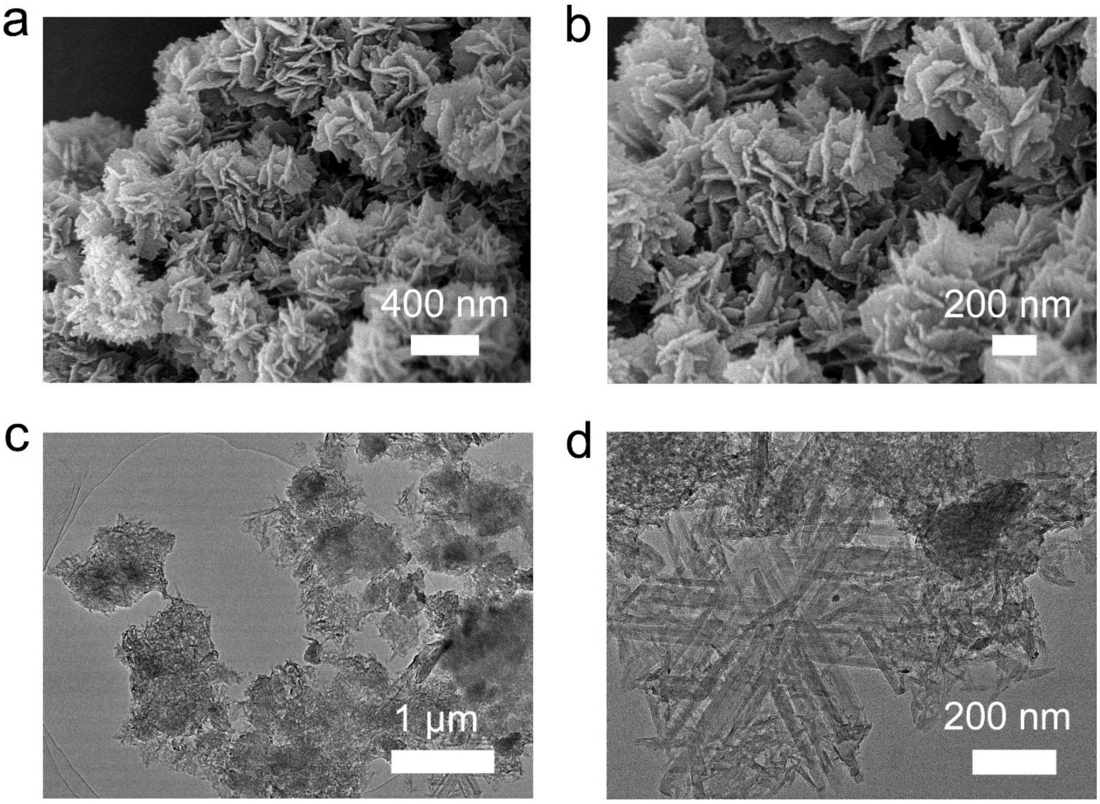

Fig. S10 (a,b) SEM and (c,d) TEM images of Cu-TABQ obtained at 90 °C.

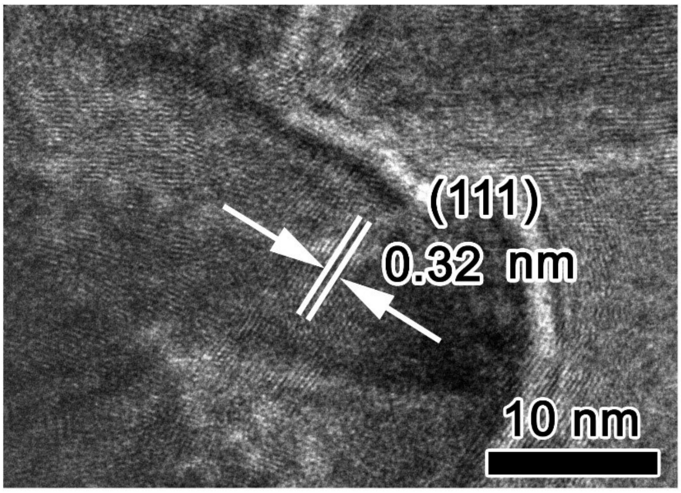

Fig. S11 HRTEM image of Cu-TABQ.

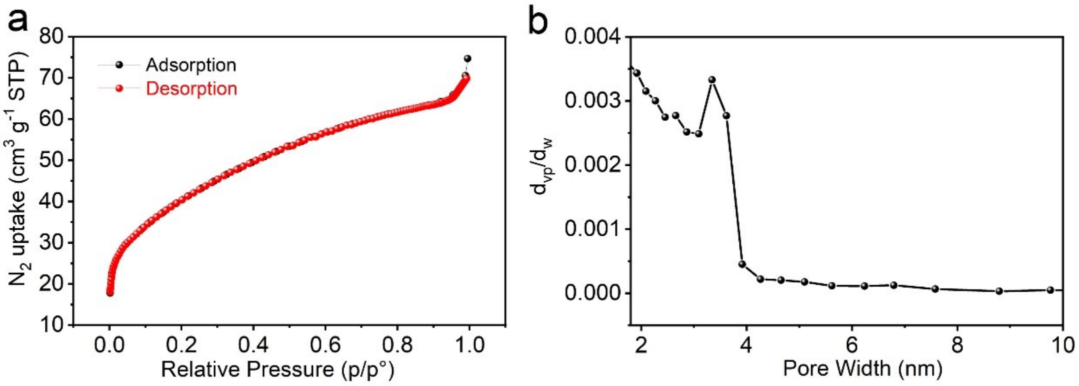

Fig. S12 (a) N_2 adsorption isotherm and (b) pore size distribution analysis of the Cu-TABQ.

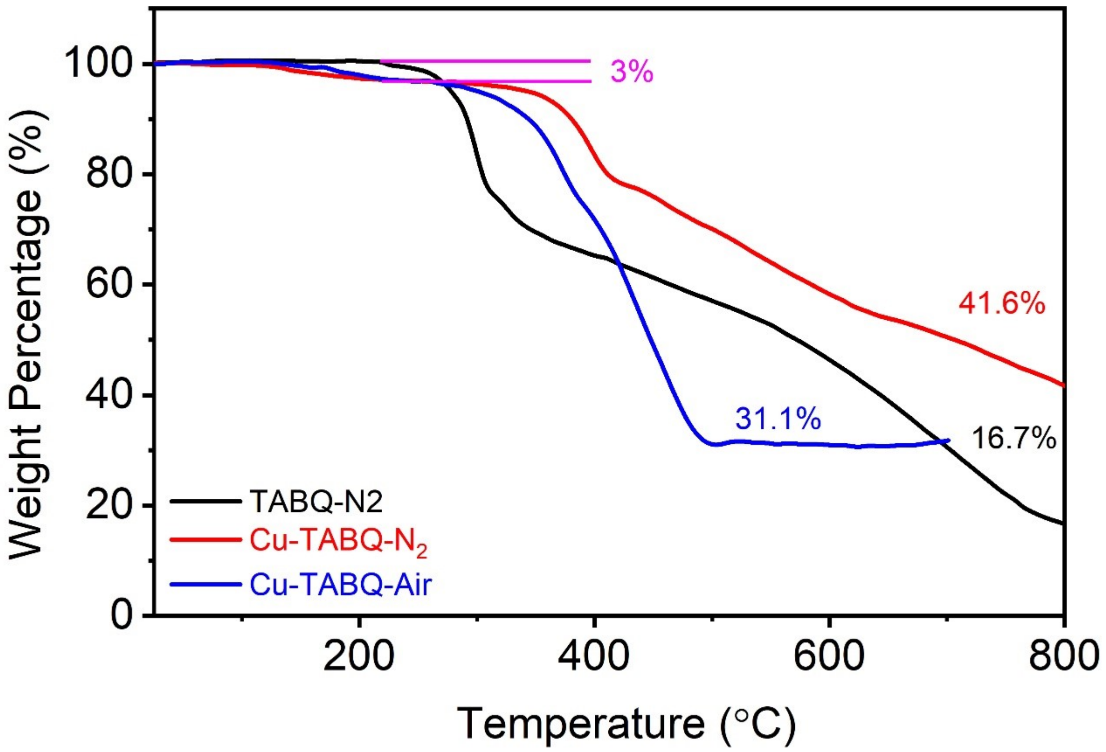

Fig. S13 TGA characterization of Cu-TABQ and TABQ.

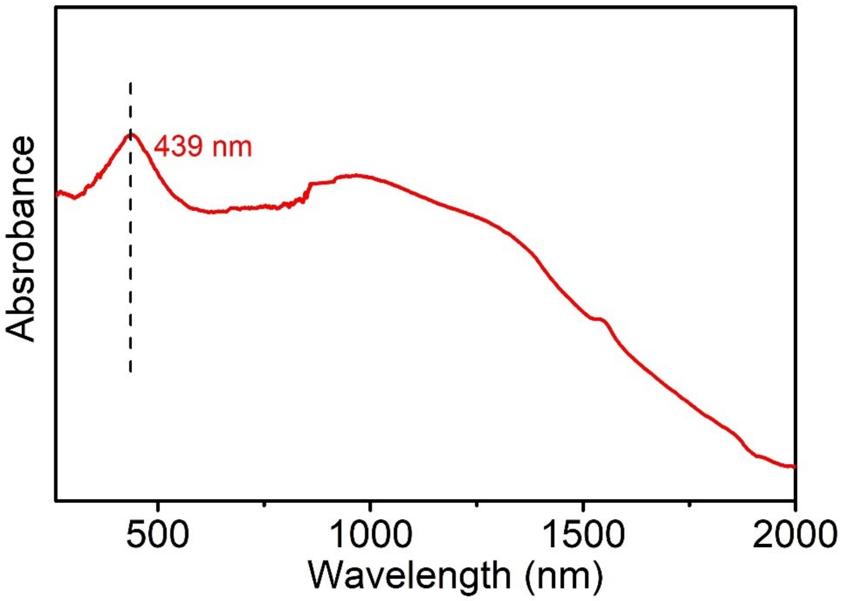

Fig. S14. UV-vis spectrum of Cu-TABQ.

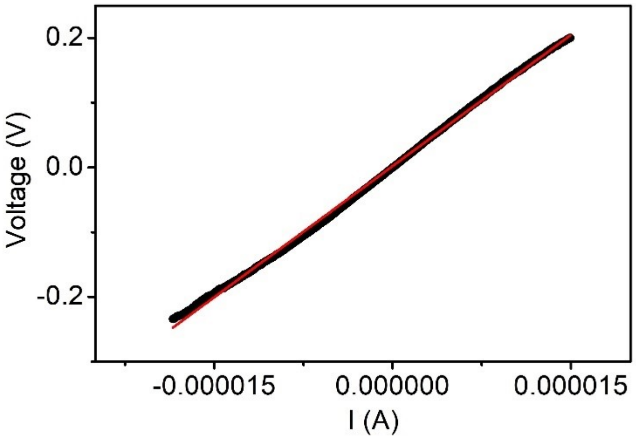

Fig. S15. Linear I-V curves of Cu-TABQ.

The electric conductivity was measured by using I-V curves, where the Cu-TABQ powder was pressed into pellets as the electrode. Based on $R = U/I = 1/\sigma \times L/A$, where R is resistance of Cu-TABQ pellet (the slope in I-V curves), σ is electric conductance, $L = 0.069$ cm is thickness of the pellet, $A = 0.5024$ cm^2 is cross-sectional area of the pellet. The resistance of the Cu-TABQ pellet is 13506 Ω. Thus, the electric conductivity of Cu-TABQ is calculated to be 1.02×10^{-3} S m^{-1}.

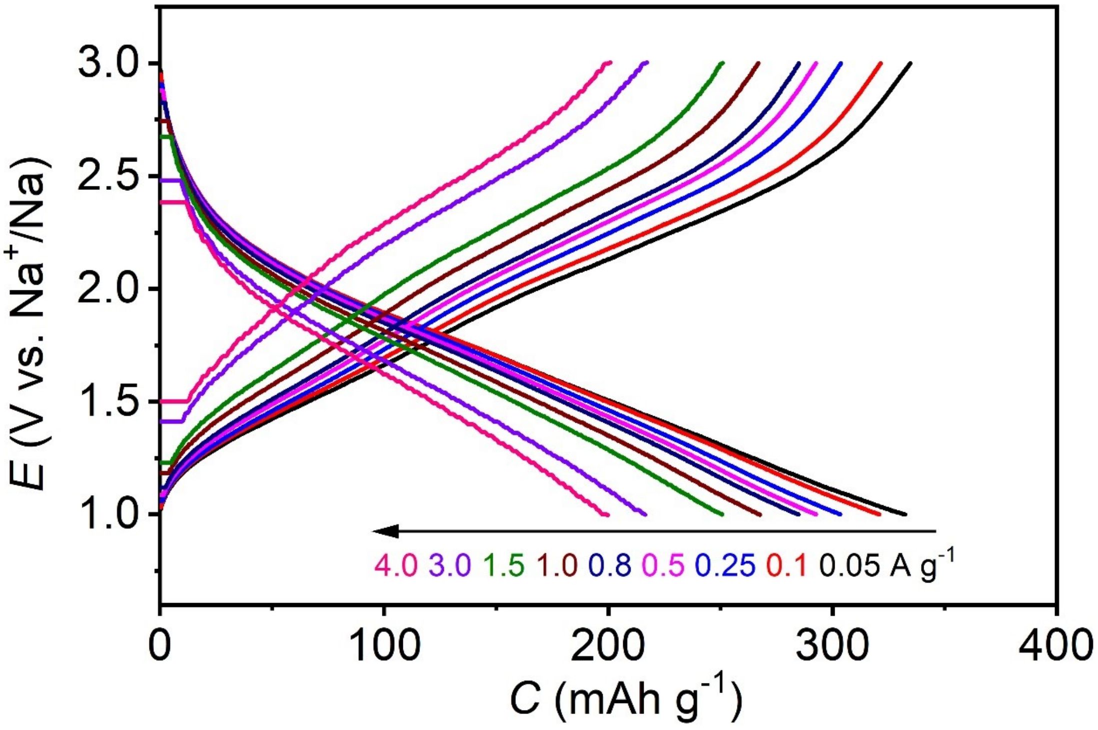

Fig. S16 Charge/discharge curves at different current densities.

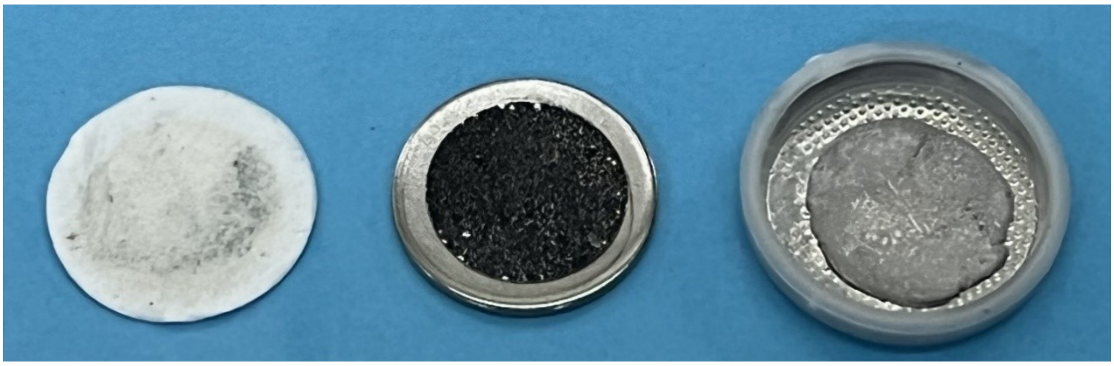

Fig. S17 Digital photos of the disassembled Na//Cu-TABQ after 200 cycles.

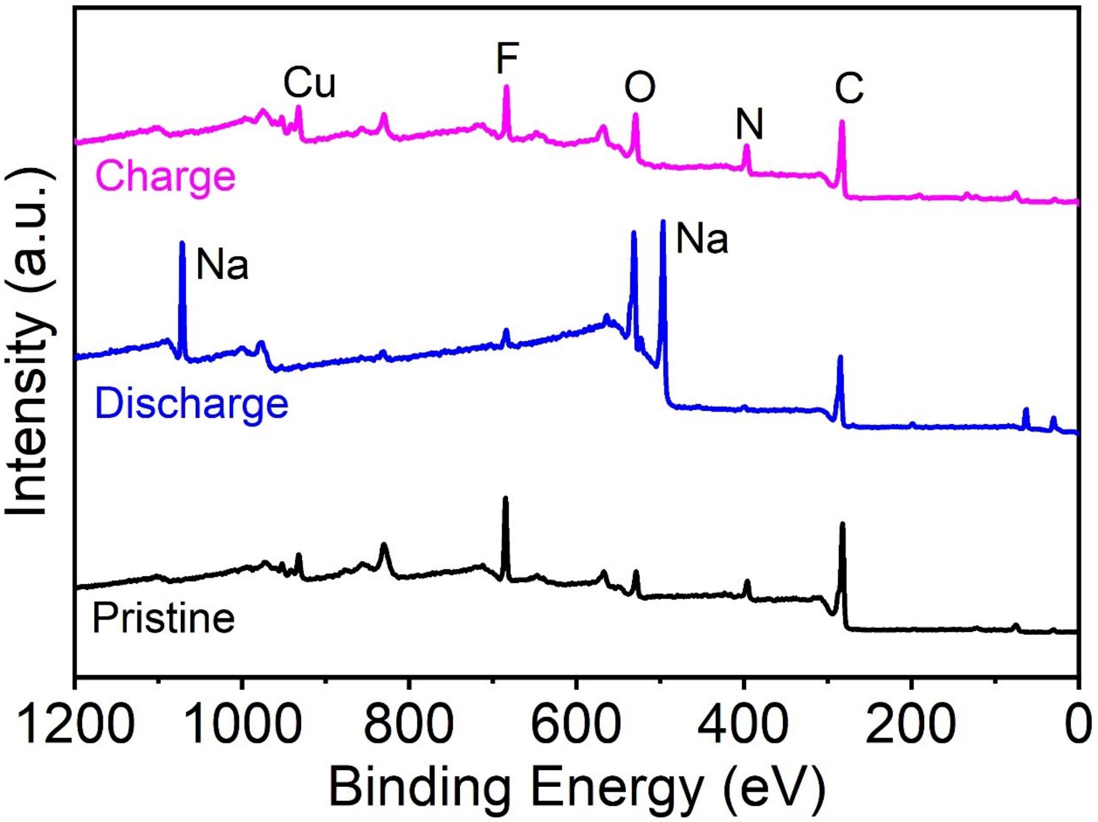

Fig. S18 Full XPS spectra of Cu-TABQ in the first discharge and charge processes.

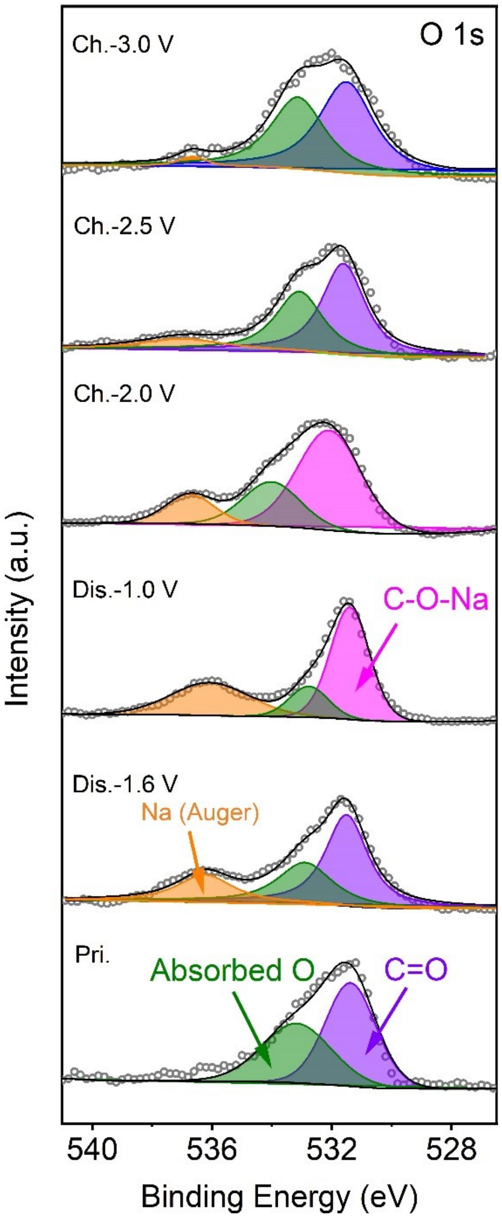

Fig. S19 *Ex-situ* O 1s XPS spectra of Cu-TABQ in the first discharge and charge processes.

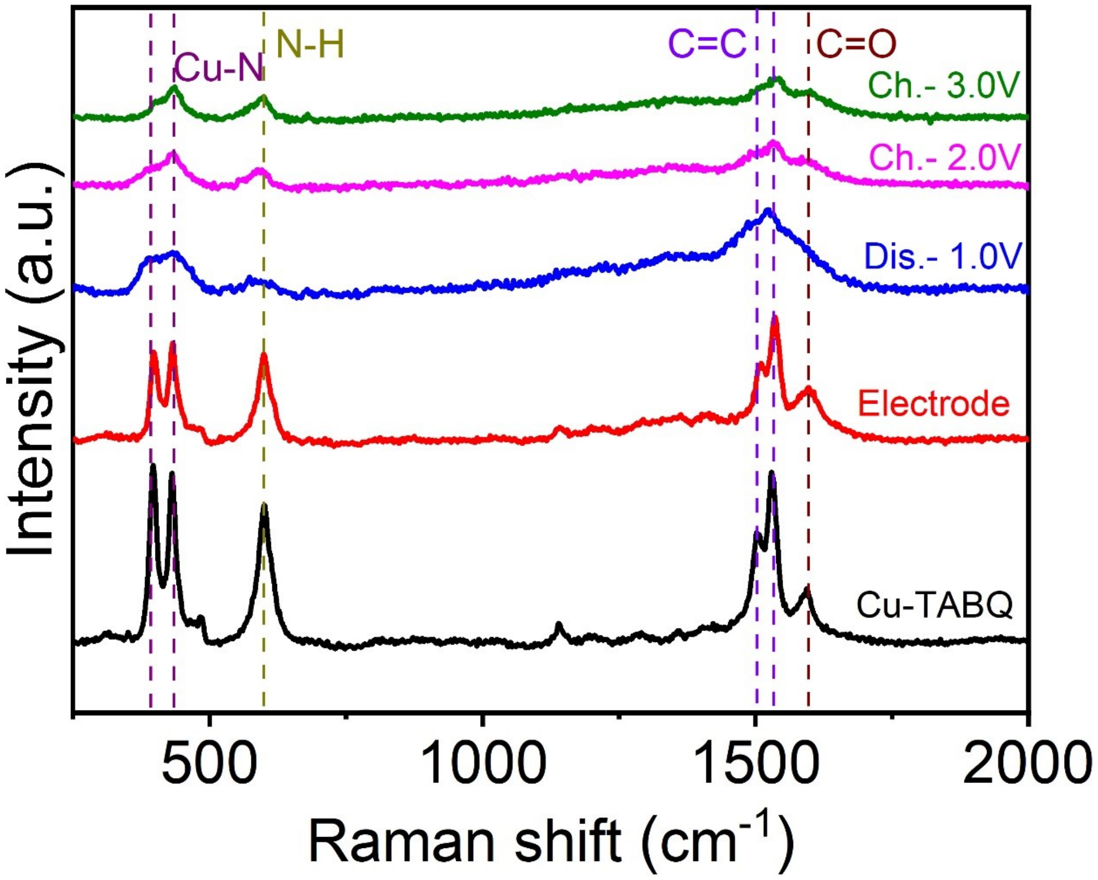

Fig. S20 *Ex-situ* Raman spectra of the Cu-TABQ electrode in the first discharge and charge process.

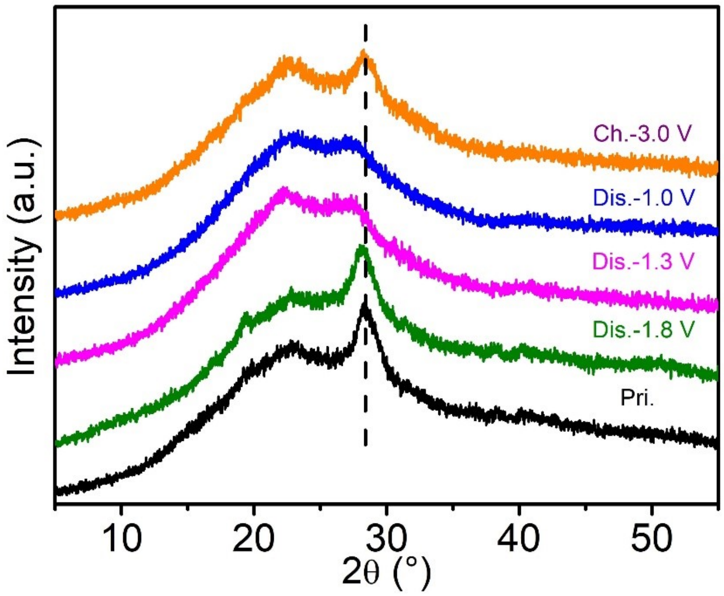

Fig. S21. XRD patterns of the Cu-TABQ electrode during the first cycle.

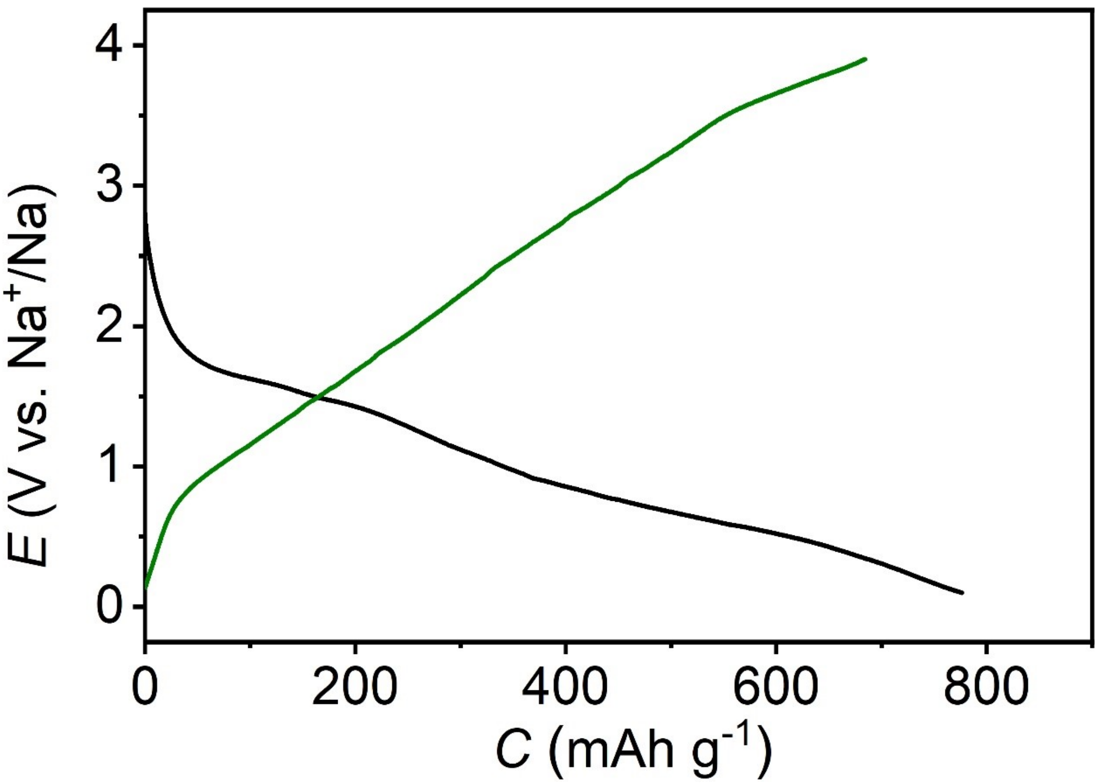

Fig. S22 Discharge/charge curves of the first cycle at 50 mA g^{-1} in the voltage range from 0.1 to 3.9 V.

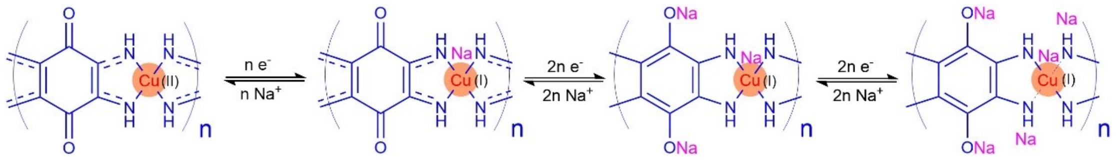

Fig. S23 Schematic diagram of insertion/extraction of Na$^+$ in Cu-TABQ in the voltage range from 0.1 to 3.9 V.

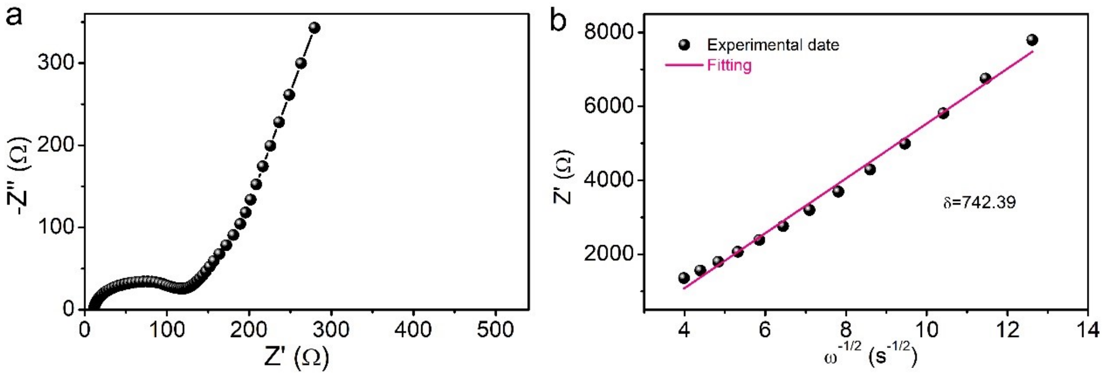

Fig. S24 EIS spectrum of Cu-TABQ at open-circuit voltage before test; (b) Relationship between Z' and $\omega^{-1/2}$ in the low-frequency of EIS of Cu-TABQ at open-circuit voltage before test.

Table S1. Atomic coordinates of Cu-TABQ.

atom	occ.	site	x	y	z
C1	1	1a	0.28329	0.60239	0.89772
C2	1	1a	0.71671	0.39761	0.10228
C3	1	1a	0.39761	0.71671	0.10228
C4	1	1a	0.60239	0.28329	0.89772
C5	1	1a	0.38332	0.38332	0.78098
C6	1	1a	0.61668	0.61668	0.21902
H1	1	1a	0.99471	0.64473	0.67734
H2	1	1a	0.00529	0.35527	0.32266
H3	1	1a	0.35527	0.00529	0.32266
H4	1	1a	0.64473	0.99471	0.67734
N1	1	1a	0.08552	0.71179	0.83319
N2	1	1a	0.91448	0.28821	0.16681
N3	1	1a	0.28821	0.91448	0.16681
N4	1	1a	0.71179	0.08552	0.83319
O1	1	1a	0.28606	0.28606	0.59362
O2	1	1a	0.71394	0.71394	0.40638
Cu1	1	1a	0	0	0

Triclinic, a=6.98253 Å, b=6.98253 Å, c=3.22703 Å, α=γ=92.2166°, β=67.5636°, V=145.2689 Å^3 (R_{wp} = 1.63%, R_p = 1.08%, χ^2 = 1.89).

Table S2. Elemental analysis (EA) results of Cu-TABQ.

Weight ratio		C%	N%	H%	(Cu+O)%
Theoretical results		**31.64**	**24.61**	**1.76**	**41.99**
Experimental results	30°C-2h	31.56	23.23	2.44	42.77
	60°C-2h	31.49	23.42	2.10	42.99
	90°C-2h	31.38	23.71	2.31	42.6

Table S3. Comparison of electrochemical performance of Cu-TABQ sample with reported Metal-organic cathodes in SIBs.

Sample	Voltage range [V vs.Na^+/Na]	Discharge capacity[mAh g^{-1}]/Current denstity[mA g^{-1}]	Rate capability (mAh g^{-1})	Capacity retention	Reference
Zn-HHTP	0.5-3.5	150/100	60/8.0 A g^{-1}	90% (1000 cycles) 0.1 A g^{-1}	S6
Co-bqdc	0.01-2.5	264/100	178/1.0 A g^{-1}	79% (1000 cycles) 0.1 A g^{-1}	S7
Ni-TTO	1.2-3.2	140/100	118/5.0 A g^{-1}	83% (100 cycles) 0.1 A g^{-1}	S8
Cu-TAPT	1.0-3.8	313.4/100	152/5.0 A g^{-1}	97% (250 cycles) 1.0 A g^{-1}	S9
CuTCNQ	2.0-4.1	255/20	/	89% (200 cycles) 0.05 A g^{-1}	S10
Mn-DHBQ	0.01-2.5	261/100	129/2.0 A g^{-1}	67% (500 cycles) 1.0 A g^{-1}	S11
NiQAP	1.0-3.5	225.6/50	99.6/5.0 A g^{-1}	91% (1000 cycles) 1.0 A g^{-1}	S12
HATN-SCu	0.01-3.0	231/100	82/5.0 A g^{-1}	100% (10000 cycles) 2.0 A g^{-1}	S13
Co-HAB	0.5-3.0	291/50	152/12.0 A g^{-1}	95% (150 cycles) 4.0 A g^{-1}	S14
O-*p*NaPC	0.01-2.0	140.7/100	56.9/2.0 A g^{-1}	87% (200 cycles) 0.2 A g^{-1}	S15
Cu-TABQ	**1.0-3.0**	**322.9/50**	**198.8/4.0 A g^{-1}**	**100% (700 cycles)** **2.0 A g^{-1}**	**This work**

Reference:

[S1] Z. Luo, L. Liu, J. Ning, K. Lei, Y. Lu, F. Li, J. Chen, A microporous covalent–organic framework with abundant accessible carbonyl groups for lithium-ion batteries, *Angew. Chem. Int. Ed.*, 2018, **57**, 9443.

[S2] G. Kresse, J. Furthmüller, Efficiency of ab-initio total energy calculations for metals and semiconductors using a plane-wave basis set *Comput. Mater. Sci.*, 1996, **6**, 15-50.

[S3] G. Kresse, J. Furthmüller, Efficient iterative schemes for ab initio total-energy calculations using a plane-wave basis set, *Phys. Rev. B*, 1996, **54**, 11169.

[S4] J. P. Perdew, K. Burke, M. Ernzerhof, Generalized gradient approximation made simple, *Phys. Rev. Lett.*, 1996, **77**, 3865.

[S5] J. P. Perdew, Y. Wang, Pair-distribution function and its coupling-constant average for the spin-polarized electron gas, *Phys. Rev. B*, 1992, 46, 12947.

[S6] Y. Chen, Q. Zhu, K. Fan, Y. Gu, M. Sun, Z. Li, C. Zhang, Y. Wu, Q. Wang, S. Xu, J. Ma, C. Wang, W. Hu, Successive storage of cations and anions by ligands of π–d-conjugated coordination polymers wnabling robust sodium-ion batteries, *Angew. Chem. Int. Ed.*, 2021, **133**, 18917-18924.

[S7] Y. Zhang, S. Yang, X. Chang, H. Guo, Y. Li, M. Wang, W. Li, L. Jiao, Y. Wang, MOF based on a longer linear ligand: electrochemical performance, reaction kinetics, and use as a novel anode material for sodium-ion batteries, *Chem. Commun.*, 2018, **54**, 11793-11796.

[S8] Y. Wu, Y. Chen, M. Tang, S. Zhou, C. Jiang, S. Zhou, C. Wang, A highly conductive conjugated coordination polymer for fast-charge sodium-ion batteries: reconsidering its structures, Chem. Commun., 2019, **55**,10856-10859.

[S9] K. Fan, J. Li, Y. Xu, C. Fu, Y. Chen, C. Zhang, G. Zhang, J. Ma, T. Zhai, C. Wang, Single crystals of a Highly conductive three-dimensional conjugated coordination polymer, *J. Am. Chem. Soc.*, 2023, **145**, 12682–12690.

[S10] C. Fang, Y. Huang, L. Yuan, Y. Liu, W. Chen, Y. Huang, K. Chen, J. Han, Q. Liu, Y. Huang, A metal-organic compound as cathode material with superhigh capacity achieved by reversible cationic and anionic redox chemistry for high-energy sodium-ion batteries, *Angew. Chem. Int. Ed.*, 2017, **129**, 6897-6901.

[S11] K. Fan, C. Zhang, Y. Chen, G. Zhang, Y. Wu, J. Zhou and C. Wang, Regulating the metal nodes of 1D conjugated coordination polymers for enhancing the performance of sodium-ion batteries, *J. Mater. Chem. C*, 2022, **10**, 2592-2599.

[S12] L. Cheng, J. Yu, L. Chen, J. Chu, J. Wang, H. G. Wang, D. Feng, F. Cui, G. Zhu, Immobilizing quinone-fused aza-phenazine into π-d conjugated coordination polymers with multiple-active sites for sodium-ion batteries, *Small*, 2023, **35**, 2301578.

[S13] B. Wang, J. Li, M. Ye, Y. Zhang, Y. Tang, X. Hu, J. He and C. C. Li, Dual-redox sites guarantee high-capacity sodium storage in two-dimension conjugated metal-organic frameworks, *Adv. Funct. Mater.*, 2022, **32,** 2112072.

[S14] J. Park, M. Lee, D. Feng, Z. Huang, A. C. Hinckley, A. Yakovenko, X. Zou, Y. Cui, Z. Bao, Stabilization of hexaaminobenzene in a 2D conductive metal-organic framework for high power sodium storage, *J. Am. Chem. Soc.*, 2018, **140**, 10315-10323.

[S15] J. Lee, Y. Kim, S. Park, K. H. Shin, G. Jang, M. J. Hwang, D. Kim, K. A. Min, H. S. Park, B. Han, D. K. P. Ng, L. Y. S. Lee, Sodium-coordinated polymeric phthalocyanines as stable high-capacity organic anodes for sodium-ion batteries, *Energy Environ. Mater.*, 2023, **4**, e12468.